Journal of Wind Engineering & Industrial Aerodynamics 180 (2018) 182–190

Contents lists available at ScienceDirect

Journal of Wind Engineering & Industrial Aerodynamics

journal homepage: www.elsevier.com/locate/jweia

Analysis of crosswind aerodynamics for competitive hand-cycling

Paul Mannion [a,b,d,*], Yasin Toparlar [b], Bert Blocken [b,c], Eoghan Clifford [a,d], Thomas Andrianne [e], Magdalena Hajdukiewicz [a,d]

[a] Department of Civil Engineering, College of Engineering and Informatics, National University of Ireland Galway, University Road, Galway, Ireland
[b] Department of the Built Environment, Eindhoven University of Technology, P.O. box 513, 5600 MB, Eindhoven, The Netherlands
[c] Department of Civil Engineering, KU Leuven, Kasteelpark Arenberg 40 – bus 2447, 3001, Leuven, Belgium
[d] Informatics Research Unit for Sustainable Engineering (IRUSE), Galway, Ireland
[e] Department of Aerospace and Mechanical Engineering, University of Liège, Allée de la Découverte, 9 Quartier Polytech 1, B52/3, B-4000, Liège, Belgium

ARTICLE INFO

Keywords:
Hand-cycling
Para-cycling
Aerodynamics
CFD simulations
Wind-tunnel experiments
Crosswinds

ABSTRACT

Competitive hand-cycling represents a unique case for cycling aerodynamics as the athletes are in a relatively aerodynamic position in comparison to traditional able-bodied cyclists. There are some aerodynamic similarities between both cycling disciplines, including wheel designs and helmets. The lack of research in hand-cycling aerodynamics presents the potential for significant improvements. This research analysed the aerodynamics of competitive hand-cycling under crosswind conditions using wind-tunnel experiments and Computational Fluid Dynamics (CFD) simulations. A range of yaw angles from 0° to 20° in 5° increments were investigated for two separate hand-cycling setups; a road race and a time-trial setup. A maximum drag increase of 14.1% was found from 0° to 15° yaw, for a hand-cyclist equipped for a road race. The three disk wheels used for the TT setup had a large impact on the lateral forces experienced by the TT hand-cyclist. At just 5° yaw and at 15 m/s, the drag and lateral forces for the TT setup matched closely, while this event did not occur until 15° yaw at the same velocity for the road setup. For 20° yaw, the ratio of the lateral force to drag force was 1.6 and 5.6 for the road and TT setups respectively.

1. Introduction

Crosswinds can be a hindrance for cyclists across all cycling disciplines. Race tactics have been developed to counter crosswind effects, such as riding in staggered formations. In addition to the drag dependence on yaw angle, another important aspect in crosswind conditions is that disk wheels can affect stability and steering (Crouch et al., 2017; Tew and Sayers, 1999). Contrary to aerofoil aerodynamics, the drag experienced by a cyclist is measured in the direction the cyclist is travelling as opposed to the stream-wise flow direction (Barry et al., 2012; Fintelman et al., 2014, 2015a).

Aerodynamic refinement is commonly the subject of scientific investigations for improved performance in cycling (Haake, 2009), with cyclist postures having received significant attention in the literature (Defraeye et al., 2010a; Fintelman et al., 2015b; García-López et al., 2008). However, crosswind analysis of able-bodied traditional cyclists has seen limited attention in the literature, even though cyclists typically experience a crosswind to some degree in all outdoor events. Concerning traditional cycling, Fintelman et al. (2015a) performed Computational Fluid Dynamics (CFD) simulations to analyse solo cycling aerodynamics under crosswind conditions, with validation data acquired from wind-tunnel experiments described by Fintelman et al. (2014). It was found that Large-Eddy Simulation (LES), by comparison to the wind-tunnel experiments, provided the best performance for drag prediction for 15° yaw with a deviation of 5%. Larger discrepancies were found by Fintelman et al. (2015a) between experimental and numerical results using other methods such as Detached Eddy Simulation (DES), with deviations from the experimental data of up to 17% between the drag forces at yaw angles of 15°.

The majority of the crosswind aerodynamics studies in cycling have focused on isolated wheel geometries (Barry et al., 2012; Godo et al., 2010; Tew and Sayers, 1999). Wind-tunnel experiments were conducted by Tew and Sayers (1999) to compare a number of wheel selections over a variety of yaw angles (0°–30°), wind speeds (30–55 km/h) and rotational velocities (corresponding to 0–55 km/h linear velocities). At 0° yaw, the drag by the disk wheel was 70% lower than for the standard spoked wheel. However, the standard thirty-six shallow rim spoke wheel had significantly lower lateral force coefficients than the other five

* Corresponding author. Department of Civil Engineering, National University of Ireland (NUI), Galway, University Road, Galway, Ireland.
E-mail address: p.f.mannion@tue.nl (P. Mannion).

https://doi.org/10.1016/j.jweia.2018.08.002
Received 28 February 2018; Received in revised form 26 July 2018; Accepted 1 August 2018
Available online 8 August 2018
0167-6105/© 2018 The Authors. Published by Elsevier Ltd. This is an open access article under the CC BY-NC-ND license (http://creativecommons.org/licenses/by-nc-nd/4.0/).

wheels tested. The disk wheel experienced a reversal in the lateral force direction (perpendicular to the direction of motion) from negative to positive in the region of 0°–8° yaw for all wind speeds, indicating a shift in the location of boundary layer separation. Godo et al. (2010) considered six isolated wheel geometries over 10 yaw angles at two velocities: 20 mph (32.19 km/h) and 30 mph (48.28 km/h). The disk wheel provided the greatest drag advantage, with the deep dish wheel in second place. However, both wheels experienced lateral forces in excess of all other wheels tested.

Wind-tunnel testing and CFD simulations have been used extensively for cycling aerodynamics and other competitive sports topics (Blocken, 2014; Crouch et al., 2017). However, to the best of our knowledge, a detailed analysis of crosswind effects on hand-cycle aerodynamics by either CFD simulations or wind-tunnel tests has not yet been published. Crosswinds can be important for performance and safety. This paper analyses the crosswind aerodynamics for a H3 category competitive hand-cyclist in a road race setup (Fig. 1a,c) and time-trial setup (Fig. 1b, d), which is relevant for categories H1-H4 due to the athlete positions adopted and the cycling equipment (UCI, 2017).

2. Wind-tunnel experiments

Wind-tunnel experiments were carried out in the aeronautical test section of the wind-tunnel laboratory at the University of Liège, Belgium, in a test chamber with cross-section dimensions $2 \times 1.5\ m^2$. A H3 competitive hand-cyclist was 3D scanned to provide the geometrical data for manufacturing a quarter-scale model (Fig. 2a). The blockage ratio reached 2.3% at the maximum yaw angle of 20°. The cyclist model was placed on a smooth horizontal platform with a sharp leading edge and raised 0.3 m from the test chamber floor to reduce the approach-flow boundary layer height (Fig. 2b). A wind speed of 60 m/s was imposed for Reynolds number similarity with a full-scale hand-cyclist at 15 m/s. 3D solid blockage corrections from (Barlow et al., 1999) applicable for blockage ratios between 1 and 10% were applied using the short-form equation by Thorn (1943) with a body shape value (K) of 0.96. A circular plate in the platform allowed yaw angle variation with five crosswind yaw angles investigated (−10°, 5°, 10°, 15°, 20°), in addition to the 0° experiment.

A six-axis Delta model force transducer (ATI, 2018) was attached to the hand-cycle model vertically in line with the model's centre of gravity (Fig. 2b). The error range was ±1.24 N at a 95% confidence interval. The error range was calculated from the calibration targets; 0.75% of the full-scale load. Force data were sampled for 180 s at a rate of 10 Hz after a 30 s settling period. Air temperature measurements inside the test chamber were used to correct force measurements to an air density at 15 °C and 101325 Pa, ensuring consistency across all experimental data and CFD simulation results. Local meteorological data was used to correct for the atmospheric pressure at the date of the experiments. A pitot tube was used to measure the stream-wise air velocity, to correct the force measurements to the desired 60 m/s velocity, for all the yaw angles tested. Previous experiments for quarter-scale cyclist models in the same wind-tunnel reported an approach-flow turbulence intensity below 0.2% (Blocken et al., 2016).

3. CFD simulations

3.1. Computational domain and boundary conditions

For the CFD validation, the simulations were performed with the same geometrical model as in the wind-tunnel experiments but in full scale, including all hand-cycle wheel supports, baseplate and platform surface in the CFD domain (Fig. 3). The platform was included as a no-slip wall. This allowed for boundary layer development on the platform as in the wind-tunnel experiments. A no-slip wall boundary condition with zero roughness was applied to the hand-cycle, supports, baseplate and platform surfaces. A cylindrical interface was used to rotate the hand-cycle geometry to the selected yaw angles. The computational domain and boundary conditions are shown in Fig. 3. The max blockage ratio for the domain at 20° was below the 3% maximum recommended (Blocken, 2015; Franke et al., 2010; Tominaga et al., 2008). A velocity of 15 m/s was imposed for all the yaw angles tested. Viscosity was 1.789×10^{-5} kg/ms and density was 1.225 kg/m^3. After the validation study, the wheel supports, baseplate and platform surface were removed from the CFD domain for more accurate predictions of hand-cycling aerodynamics, see section 4.2.

3.2. Solver settings

The commercial CFD code ANSYS Fluent 16 (ANSYS Fluent, 2015) was used to solve the 3D Reynolds-averaged Navier–Stokes (RANS) equations using two turbulence models for closure: the 1-equation Spalart-Allmaras model (Spalart and Allmaras, 1992) and the 2-equation Shear Stress Transport (SST) k-ω model (Menter, 1994). The pseudo-transient implicit under-relaxation method was used with a time-step of 0.01 s, using the Coupled algorithm for pressure-velocity coupling, and the Least Squares Cell Based method to compute gradients. Aerodynamic forces were averaged at every pseudo-time-step over a period of 4000 steps. Second-order discretisation schemes were used throughout along with second-order pressure interpolation. The maximum values for the scaled residuals were: 1×10^{-5} for continuity, 1×10^{-7} for momentum, 1×10^{-4} for turbulent kinetic energy, 1×10^{-4} for specific dissipation rate and 1×10^{-6} for turbulent eddy viscosity where the Spalart-Allmaras turbulence model was used.

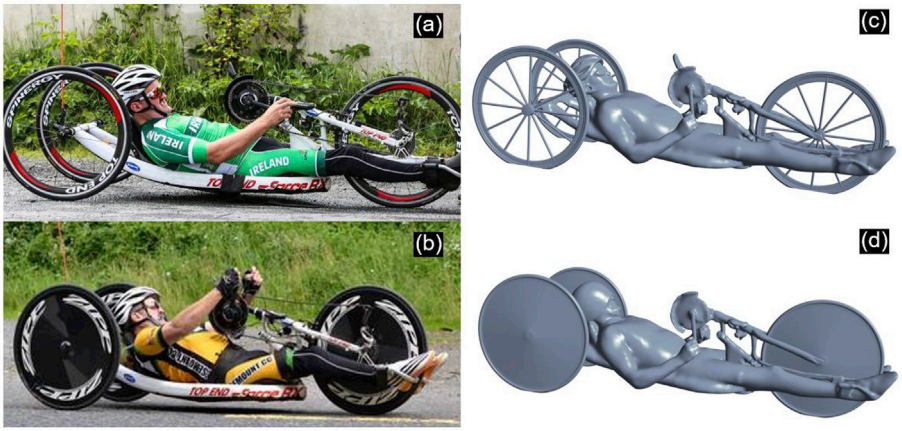

Fig. 1. Photos of an Irish H3 category hand-cyclist with spoked wheels for a road race, and (b) disk wheels for a TT event. (Photos copyright of Sportfile, Cycling Ireland and Paralympics Ireland, reproduced with permission). Part (c) and (d) illustrate the geometries used for this study to represent (a) and (b) respectively.

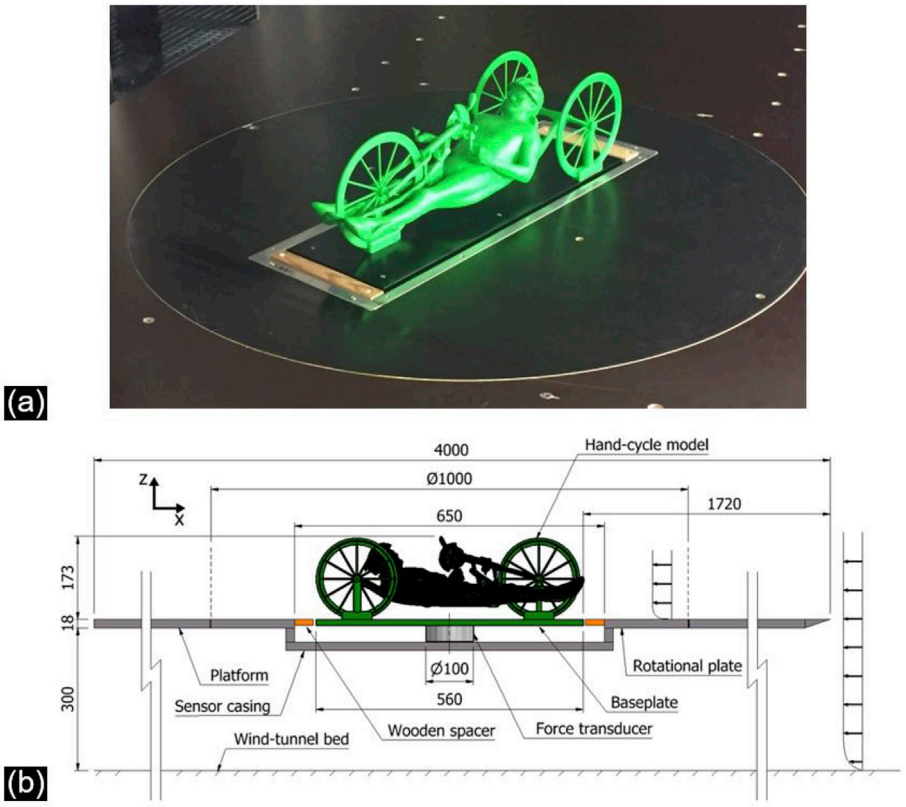

Fig. 2. (a) Photo of manufactured model at 20° yaw in the wind-tunnel. (b) Corresponding schematic of scaled hand-cycle model attached to transducer on rotational plate. Units are in mm.

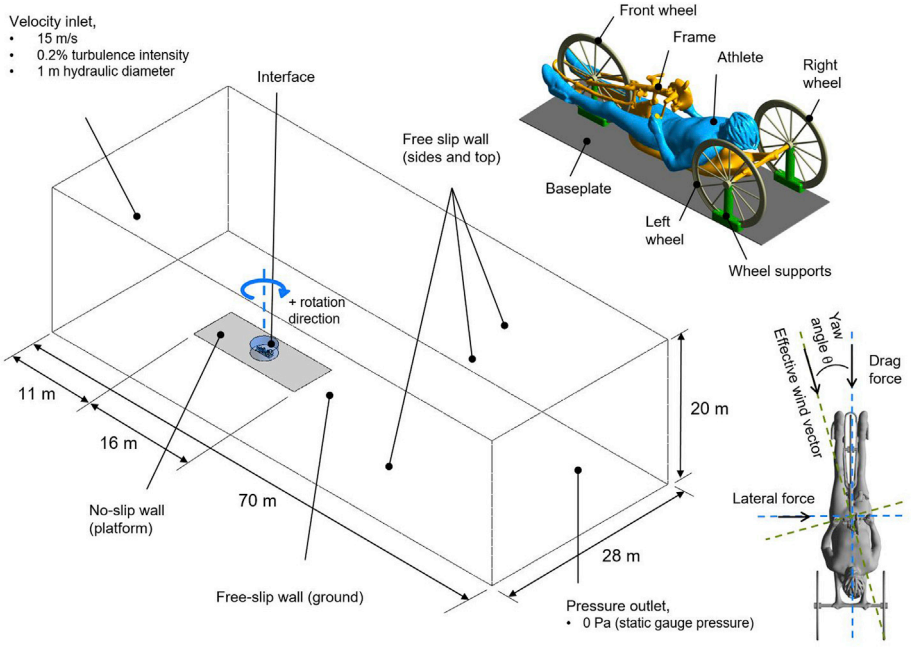

Fig. 3. Computational domain, boundary conditions and breakdown of primary hand-cycle geometry components.

3.3. Computational grid

A systematic grid sensitivity analysis of three grids named grids 1–3 (with 77.4, 27.3 and 10.4 million cells) was conducted on the hand-cycle geometry to determine the grid resolution for a fourth grid named grid 4 (25,721,804 cells) which balanced computational effort and accuracy. Grid Convergence Index (GCI) (Roache, 1997) values of 0.29% and 1.29% were obtained for grids 1 and 2 respectively. Grid 4 contained a cylindrical interface to allow for the rotation of the hand-cycle geometry. The cell face size on the cylinder interface surfaces was fixed at 0.02 m, to ensure that interpolation error was kept to a minimum between the two face zones. Twenty prism layers were used in grid 4 with a first layer

height of 2.5×10^{-5} m applied to the hand-cycle geometry, wheel supports and baseplate, yielding an average y* value of 0.8. Five prism layers were applied to the platform surface. Note that y^* was used instead of y^+, as recommended by Blocken and Toparlar (2015) for grids used in cycling studies. y^+ is defined as follows:

$$y^+ = \frac{u^+ y_P}{\nu} \tag{1}$$

where ν is the kinematic viscosity [m^2/s] and y_P [m] is the normal distance from the wall to the centre point P of the first cell. u^+ [m/s] is the friction velocity, defined by:

$$u^+ = \sqrt{\frac{\tau_w}{\rho}} \tag{2}$$

where ρ [kg/m^3] is the density of the fluid in the wall bounded flow and τ_w [Pa] is the wall shear stress. On the other hand, y^* is defined as:

$$y^* = \frac{u^* y_P}{\nu} \tag{3}$$

where the friction velocity u^* [m/s] is defined as:

$$u^* = C_\mu^{\frac{1}{4}} k_P^{\frac{1}{2}} \tag{4}$$

where C_μ [-] is a model constant, and k_P [m^2/s^2] is turbulent kinetic energy at P.

While both definitions will often provide very similar values, y^* is used within this research instead of y^+. As discussed by Blocken and Toparlar (2015), the formulation for y^* holds an advantage over y^+ for cycling aerodynamics applications. y^* does not go to zero if the shear stress (present in equation (2)) is zero, such as in locations of flow stagnation and flow reattachment which occur in cycling aerodynamics. Therefore y^*, as opposed to y^+, can be used to specify the grid requirements in these locations. The y^* distribution on the hand-cyclist is illustrated in Fig. 4.

Grid 4 represented the hand-cycle geometry with the wheel support structures, baseplate, and platform surface from the wind-tunnel experiments (Fig. 5a), to provide good comparisons for validation purposes. However, it was desired to investigate the aerodynamics of hand-cycling without the influence of these components. Thus, using the same cell sizings, two additional grids were created, grid 5a and 5b, for a more accurate geometrical representation of hand-cycling without the

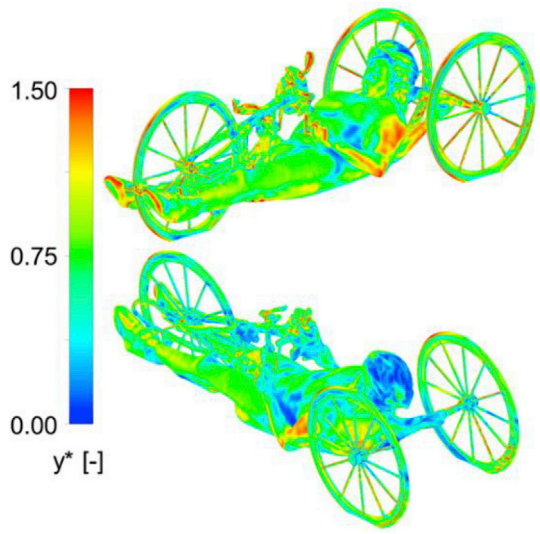

Fig. 4. y^* distribution on hand-cyclist.

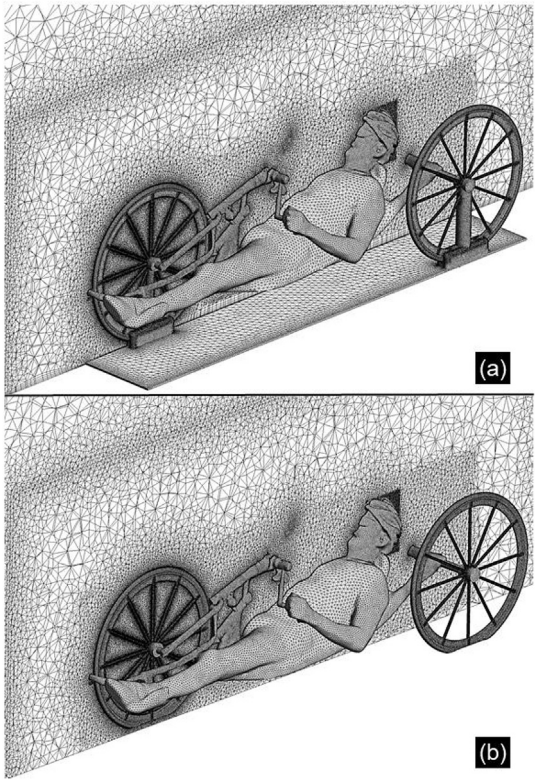

Fig. 5. Part of the surface and volume grid for (a) grid 4, and (b) grid 5a. Total cell counts are 25,721,804 and 28,189,933, respectively.

structural wheel supports, baseplate, and platform surfaces. Grid 5a (28,189,933 cells) represented a hand-cyclist in a road race setup similar to the geometry used in the wind-tunnel experiment (Fig. 5b). Grid 5b (11,013,008 cells) represented a TT setup, where disk wheels and a TT helmet were used. Fewer computational cells were required for the TT setup due to the replacement of the small geometric details from the three spoked wheels and detailed road helmet with disk wheels and a streamlined TT helmet respectively.

4. Results

The target parameters were drag area, lateral force area and pressure coefficient. Note that the 'lateral force area' was defined as the lateral force normalised by the freestream dynamic pressure in analogy with the definition of the drag area. The frontal area was 0.261 m^2 for the TT setup and 0.247 m^2 for the road setup. The projected lateral area was 0.727 m^2 for the road setup and 0.987 m^2 for the TT setup. The drag area [m^2] and lateral force area [m^2] were calculated with the following:

$$C_D A_F = \frac{F_D}{0.5 \rho V^2} \tag{5}$$

$$C_S A_S = \frac{F_S}{0.5 \rho V^2} \tag{6}$$

where F_D is the drag force [N], F_s is the lateral force [N] where the letter 'S' refers to side or lateral, V is the free-stream velocity [m/s], ρ is the air density [kg/m^3], A_F is the frontal area [m^2] with reference to the drag axis (Fig. 3), A_s is the side area [m^2] with reference to the lateral force axis of the hand-cycle (Fig. 3). The lateral force coefficient [-] was defined as:

$$C_S = \frac{F_S}{0.5 \rho A_S V^2} \tag{7}$$

where it was used to normalise lateral force data in the form of $C_S A_F$.

The pressure coefficient [-]:

$$C_P = \frac{\Delta P}{0.5\rho V^2} \tag{8}$$

where ΔP is the difference between local static pressure and upstream reference static pressure [Pa].

4.1. Validation study

The drag and lateral force data across the yaw angles tested (−10°, 0°, 5°, 10°, 15° and 20°) from the experimental results and numerical results utilising grid 4, are plotted in Fig. 6a–b. Both the SST k-ω and Spalart-Allmaras turbulence models provided good agreement with the wind-tunnel results. The root-mean-square (RMS) error was used as the performance indicator for both turbulence models against the wind-tunnel experiments. The RMS error was calculated by:

$$RMS\ Error = \sqrt{\frac{\sum_{i=1}^{n}(F_{WT_i} - F_{CFD_i})^2}{n}} \tag{9}$$

where F_{WT} is the force [N] measured in the wind-tunnel experiments, F_{CFD} is the force [N] prediction from the CFD simulations, and n is the number of yaw angles tested.

RMS errors were calculated separately for both the drag and lateral forces, from the yaw angles of −10°, 0°, 5°, 10°, 15° and 20°. Thus, an indicator was provided for the prediction of the drag and lateral forces individually for both turbulence models. RMS errors of 0.96 N and 1.48 N were calculated for the predictions of drag and lateral forces for the SST k-ω model. The Spalart-Allmaras turbulence model drag and lateral force predictions resulted in RMS errors of 1.96 N and 1.56 N respectively. Both turbulence models provided satisfactory predictions. However, the SST k-ω turbulence model was chosen for further simulations because of its slightly better performance than the Spalart-Allmaras model, and due to its good performance in prior cycling studies reported in literature. Defraeye et al. (2010b) conducted a turbulence model sensitivity analysis for an able-bodied cyclist, and determined that the SST k-ω model provided the best overall performance, with drag and lift forces predicted within 4% and 11% respectively. A turbulence model sensitivity analysis was also conducted for tandem cycling by Mannion et al. (2018), who determined that the SST k-ω model was the most suitable for tandem cycling with drag deviations of 4.0% and 4.2% for the front and rear athletes respectively. For comparison, in this study the minimum and maximum drag deviations with the SST k-ω model were 1.4% and −5.4% at 0° and 10° yaw respectively.

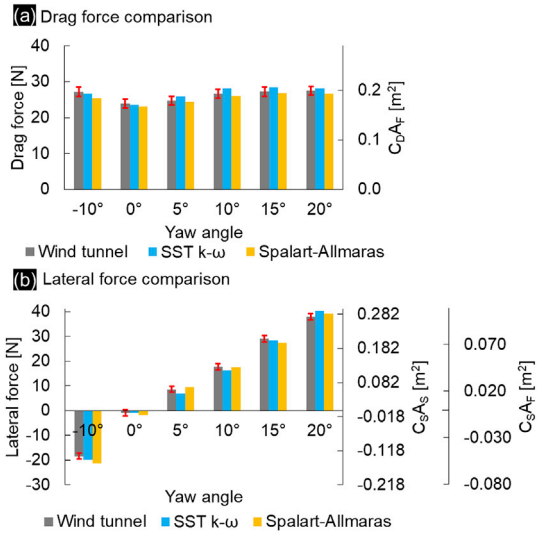

Fig. 6. Experimental and numerical (a) drag, and (b) lateral forces for the hand-cyclist for investigated yaw angles. Error bars (±1.24 N) of systematic and random errors combined within a 95% confidence interval are provided for the experimental results. Both force [N] and normalised force in $C_D A_F$, $C_S A_S$ and $C_S A_F$ terms [m^2] are provided, where C_S [-] is defined in equation (7).

4.2. Crosswind aerodynamics

Following the validation study, the crosswind aerodynamics were further investigated by removing the supporting structures for the wheels, the baseplate and the platform. The SST k-ω turbulence model was used for closure as per the validation study in section 4.1. Crosswind effects at yaw angles of 0°, 5°, 10°, 15° and 20° were investigated for two hand-cycle setups; a road setup as per the validation study with spoked wheels and a standard helmet for the athlete (grid 5a), and a TT setup with disk wheels and an aero helmet for the athlete (grid 5b). The yaw angle of −10° was not investigated further due to the near symmetry between −10° and 10° (Fig. 6), with differences of 2.1% between the wind-tunnel predictions for the drag forces, and 3.8% for the lateral forces. The wheels were modelled as stationary within the CFD simulation. The resulting $C_D A_F$ [m^2] and $C_S A_S$ [m^2] for both setups are provided in Fig. 7a–b.

The drag experienced by the hand-cyclist increased with the change in yaw angle from 0° to 15° for the road setup, and from 0° to 5° for the TT setup; by 14.1% and 3.3% respectively. The TT hand-cyclist setup experienced a lesser increase in drag than the road setup counterpart under crosswind conditions. This was expected due to the influence of the disk wheels, as per the findings for disk and spoked wheels by Tew and Sayers (1999) and Godo et al. (2010) under yaw conditions. At 20° yaw, a drag reduction of 4.1% and 6.2% was found for the road and TT setups, compared to 15° yaw. A $C_D A_F$ of 0.1322 m^2 was found at 5° and 0.1320 m^2 at 10° yaw for the TT setup, indicating a stable drag region at this yaw range.

The reduction in drag at 20° compared to 15° found by the CFD simulations for the road setup was not replicated by the wind-tunnel experiments, which had resulted in a 0.9% increase in drag between 15° and 20°. However, CFD simulations with the wheel supports, baseplate and platform surfaces included, yielded drag forces within the error range of the sensors used (±1.24 N). It is possible that a reversal in drag propagation could have been found at higher yaw angles in the wind-tunnel if they had been tested. In addition, the flow interference from the wheel supports might also have been a contributing factor to this finding.

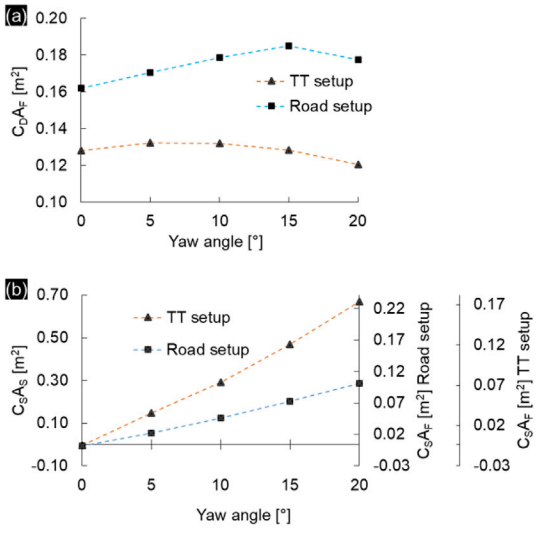

Fig. 7. (a) Drag areas and (b) lateral force area for both the road and TT hand-cycle setups.

The C_SA_S increased monotonically as the yaw angle increased. As the hand-cycle geometry was close to being symmetrical in the lateral plane, low C_SA_S values were observed at 0° yaw for the road and TT setups respectively (Fig. 7b); 3.2% and 3.7% of the drag forces for each setup respectively at the same yaw angle. At 20° yaw, the TT setup experienced a lateral force 134.0% greater than the road setup, indicating potential impact to the stability of the hand-cyclists. This increase was due to the three disk wheels in the TT setup, which were the major geometrical differences between the road and TT setups.

Roll and yaw moments were investigated to further determine the impact of aerodynamics on the stability of a hand-cyclist. The yaw moment was investigated about a vertical axis located at the centre between the front and rear wheels (Fig. 8a), as defined by Crouch et al. (2017) for cycling applications. The roll moment was investigated about an axis on the ground plane intersecting the theoretical points of contact between the ground plane and the front and right (rear) wheels (Fig. 8a). The roll and yaw moment coefficients [-] were defined respectively as:

$$C_{M:R} = \frac{M_R}{0.5\rho A_F V^2 L} \quad (10)$$

$$C_{M:Y} = \frac{M_Y}{0.5\rho A_F V^2 L} \quad (11)$$

where M_R is the roll moment [Nm], M_Y is the yaw moment [Nm], and L is the length [m] between the front and rear wheels in the drag axis (Fig. 3).

The trend for roll moment coefficient experienced by the road and TT setups (Fig. 8b) followed the same trend as the lateral forces (Fig. 7b), throughout the yaw range tested. Similar slopes for were found between the lateral force trends and the roll moment trends between 0° and 20° yaw for the road and TT setups respectively, confirming the impact of high lateral forces from disk wheels on the hand-cyclist by comparison to spoked wheels. The variation in yaw moment as the yaw angle increased was smaller than the impact of increasing yaw angle on the roll moment (Fig. 8b). Again, the disk wheels for the TT setup contributed to an increase in yaw moment by comparison to the spoked wheels of the road setup. However, the absolute difference between the maximum yaw moment coefficients at 20° for the TT and road setups was less than half the difference in roll moment coefficients at the same yaw angle; differences of 0.172 [-] and 0.351 [-] respectively. It is not expected that the increase in yaw moment due to the disk wheels would significantly influence the stability or the steering of the hand-cyclist. This is due to the additional friction provided by the two rear wheels of the hand-cycle, and due to the near-horizontal steering axis of the hand-cycle which limits the impact of the aerodynamic yaw moment on the steering of the front wheel by comparison to a traditional bicycle.

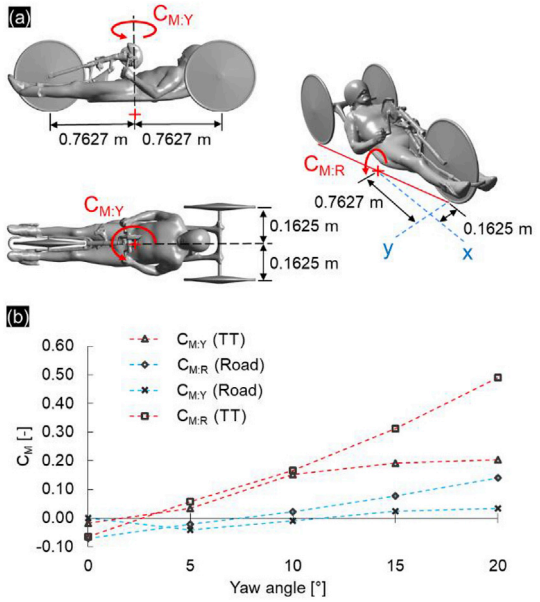

Fig. 8. (a) Moment axes and locations defined. (b) Roll and yaw moment coefficients for the road and TT hand-cycling setups at different yaw angles.

Fig. 9 provides further insight into the aerodynamics of the road and TT hand-cycle setups throughout the various yaw angles tested. The flow field is illustrated with streamlines, and with pressure coefficient contours on the surfaces of the athlete and hand-cycle. The impact of the disk wheels on the flow-field over the hand-cyclist is illustrated by the difference in streamlines for the various yaw angles, which indicate the impact to the flow from the disk wheels (Fig. 9b). This was not the case with the road setup for the hand-cycle, where the spoked wheels added some additional turbulence, but the direction of the flow was not impacted to the same degree as in the TT setup (Fig. 9a). A larger pressure coefficient was experienced on the left leg of the athlete in the TT setup at 20° yaw, in comparison to the road setup at the same angle. This was due to the difference in wheel geometries for the road and TT setups. For the TT setup, the disk wheel at the front of the hand-cycle blocked the air from flowing through the open volume that would typically be present with spoked wheels (road setup), creating a larger pressure differential on both sides of the wheel at higher yaw angles, thus impacting the leg geometry at both sides of the wheel.

The yaw angle of 20° was investigated further, as illustrated in Fig. 10a–b, with contours of the static pressure coefficient and the normalised velocity on a horizontal plane. The impact of the wheel geometry is illustrated in this comparison, with the flow passing through the open spoked wheel geometry, but diverted with solid disk wheel geometries. The direction of the wake flow from the TT setup makes evident the redirection of the flow as a result of the disk wheels. Low pressure regions between the athlete and disk wheels (Fig. 10a) resulted in high local velocities (Fig. 10b). These high local velocities induced large suction, both downwind of the front disk wheel and downwind of the wind-exposed rear wheel, and downwind of the athletes' upper body. The pressure distributions on the disk and spoked wheel surfaces at 20° yaw are illustrated in Fig. 10c. The front wheel and left wheel (both disk and spoked) were found to have the largest variations and peaks in over-pressure and under-pressure of the three hand-cycle wheels, due to the exposure of both wheels to the free-stream velocity under the yaw angles tested. By comparison, the right wheels (disk and spoked) were found to have lower pressure-coefficient variations across its geometry, due to being immersed in the wake of the hand-cyclist.

4.3. Breakdown of forces

Fig. 11a–b compares the drag and lateral forces for the hand-cycle (frame and wheels) and athlete individually for both the road and TT setups, across all yaw angles tested. There was limited variation in the relative contributions of the hand-cycle and the athlete to the total drag across each yaw angle (Fig. 11a). This suggests that drag optimisations performed for 0° yaw may be valid for all yaw angles. The athlete and hand-cycle contributed to an average of 31.7% and 68.3% to the total drag for the road setup, and 46.0% and 54.0% for the TT setup. There was more variation in athlete and hand-cycle contributions to the total lateral force throughout the yaw range tested (Fig. 11b). This was partly due to the small lateral forces at 0° yaw. However, a trend emerged between 5° and 20° yaw for both hand-cycle setups with increasing contributions from the athlete to the total lateral force and decreasing contributions from the hand-cycle geometry. At 20°, the athlete contributed 31.1% to the total lateral force for the road setup, and 10.0% for the TT setup.

5. Discussion

This research found that the drag force of a hand-cyclist in a road setup can increase by 14.1%, for increasing yaw angles from 0° to 15°.

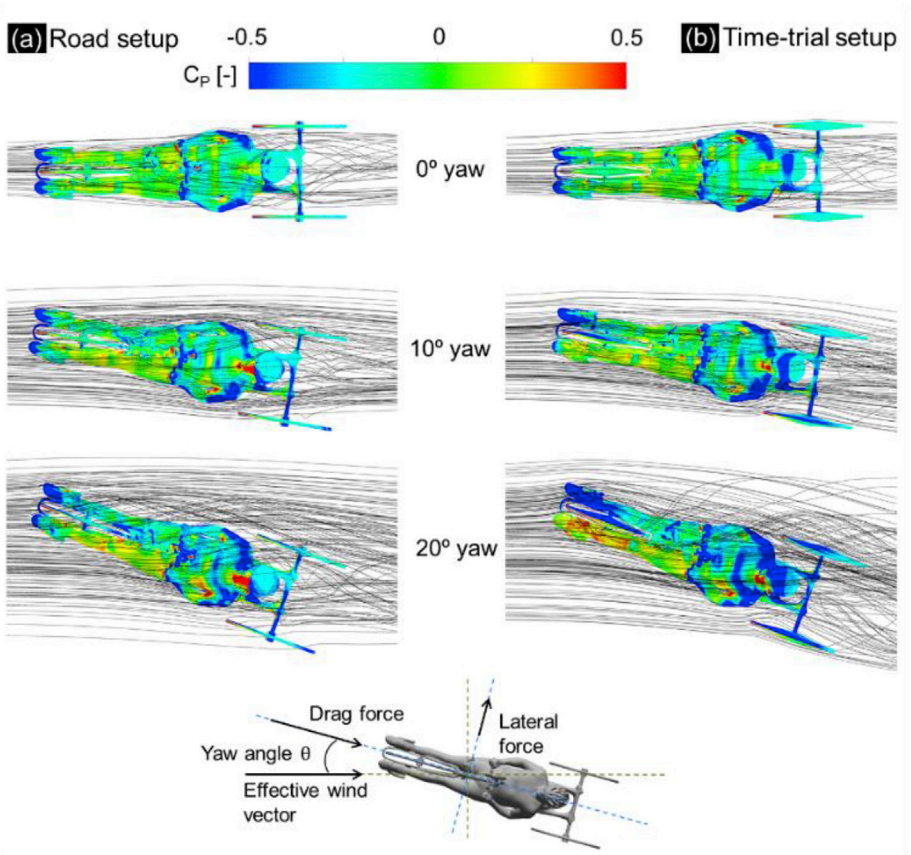

Fig. 9. Pressure coefficient contours and streamlines at yaw angles of 0°, 10° and 20° for both the road setup and TT setup.

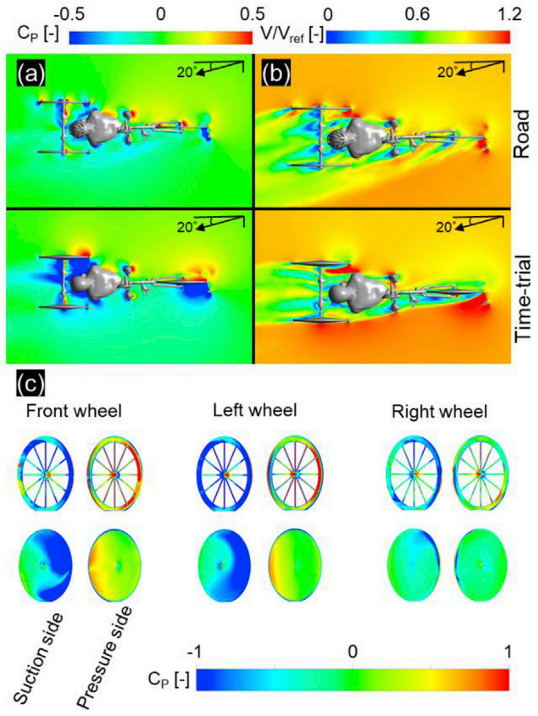

Fig. 10. Contours in a plane at mid-wheel height at 20° yaw for (a) static pressure coefficient, and (b) normalised velocity, where V_{ref} is the reference velocity of 15 m/s. (c) Pressure coefficient contours on the suction and pressure side of the wheels at 20° yaw.

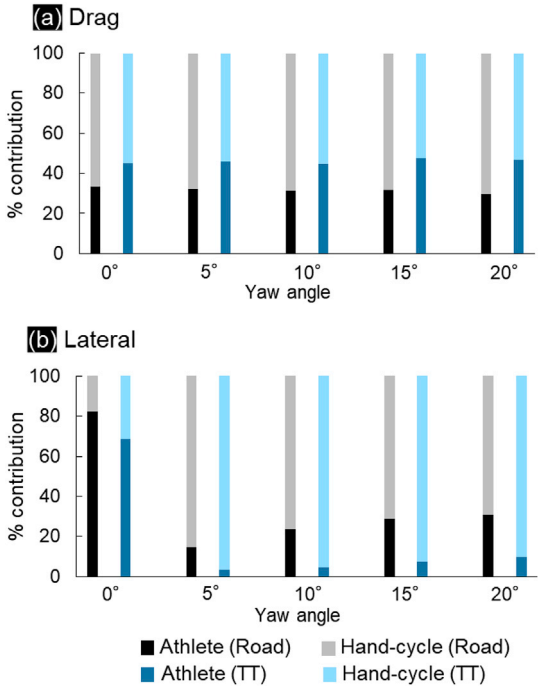

Fig. 11. Percentage contributions to the drag (a) and lateral (b) force by the hand-cycle and the athlete in the road and TT setups.

The TT setup experienced a maximum increase in drag force of 3.3% from 0° to 5° yaw. The drag recorded at 15° returned to the equivalent level of drag at 0° yaw (0.4% difference) for the TT setup, and was reduced by a further 6.2% between 15° and 20°. The road setup also experienced a 4.1% decrease in drag from 15° to 20° yaw. However, the drag force at 20° yaw was 9.5% higher than the 0° yaw prediction for the road setup. Maximum drag values were found at 15° and 5° yaw for the road and TT hand-cycling setups respectively. A similar result was found by Fintelman et al. (2015a) who reported that the drag coefficient for a regular cyclist reaches its max at 15° yaw; spoked wheels were used in this study as per the road hand-cycle setup where 15° was found to bthe critical angle for drag.

A large difference was found between the C_SA_S of the road and TT hand-cycle setups. The lateral force for the road setup at 20° yaw was 1.6 times larger than the drag force. However, the lateral force played a larger role in the aerodynamics of the TT setup, 5.6 times the drag force at 20° yaw. An evaluation of the roll moments revealed that the TT setup was more susceptible to roll than the road setup due to the disk wheels. However, the higher yaw moments resulting from the disk wheels in the TT setup were not expected to have a significant impact on the stability of the hand-cyclist. Hand-cyclists are not as easily influenced by crosswinds in terms of steering-stability as able-bodied traditional riders. This is due to the presence of three wheels in contact with the ground instead of two, combined with a low centre of gravity. Hence, the higher lateral forces might not have a negative effect on the performance of the hand-cyclists, when using disk wheels to attain better drag performance. Further research is required using track measurements or wind tunnel experiments to confirm this.

Fintelman et al. (2014) found up to 61% of the lateral force experienced by an able-bodied cyclist was attributed to the bicycle (road setup) at large yaw angles of up to 90°. This present study showed that for a road hand-cycling setup, the hand-cycle itself can contribute up a minimum of 17.9% at 0°, and a maximum of 85.4% at 5° to the total lateral force (Fig. 11b), exceeding that of a road bicycle for able-bodied users. Limited variation was found in percentage contributions of athlete/hand-cycle (for the road and TT setups) to the total drag at varying yaw angles (Fig. 11a). However, the hand-cycle (frame and wheels) contributed significantly more to the lateral forces than the athlete, throughout all the yaw angles tested (excluding 0°). In addition, the hand-cycle contributed more to the drag force than the athlete for all yaw angles, indicating that aerodynamic optimisation of the hand-cycle design and wheel choice instead of the athlete could yield greater benefits.

Simplifications in this study should be taken into account for drag/lateral force comparisons and for future research. The geometries used in the CFD simulations and in the wind-tunnel experiments contained static geometries. The surface of the athlete's geometry was smoothed to remove folds in his apparel which would have negatively impacted the grid generation. Small geometric details, such as cables, chain, and the sprocket were neglected. All surfaces in the CFD simulations were assumed to be smooth walls with zero roughness, where in reality, these surfaces would have some degree of roughness.

The arm rotation of the athlete is also expected to have an impact on the drag and lateral forces in different crosswind scenarios. The athletes' arms rotate together symmetrically at the same crank angle, instead of being 180° apart as per a traditional bicycle. The upper torso and head of the athlete along with the left and right rear wheels are located downstream of the hand-cycle cranks, and the interference drag from the rotating arms is expected to vary with the crosswind angle. Despite the legs of a traditional able-bodied cyclist not being upstream of the torso and head like the hand-cycle case, Griffith et al. (2014) found that the leg rotation impacted the drag on the athlete's torso, and thus an equivalent or larger impact could be expected for hand-cyclists.

6. Conclusion

This study investigated the aerodynamics of road and TT hand-cycling setups under crosswind conditions. Wind-tunnel experiments were used to validate the CFD simulation results for yaw angles of −10°, 0°, 5°, 10°, 15°, and 20°. Two turbulence models were considered, the Spalart-Allmaras and the SST k-ω, and simulations using both models provided good agreement with the wind-tunnel results. However, using RMS error as a performance indicator for drag and lateral force predictions over a range of yaw angles, the SST k-ω turbulence model provided more accurate predictions and is thus recommended for future research.

Following the validation study, additional CFD simulations were performed investigating the crosswind effects on hand-cyclist geometries equipped for road race and TT events. The results demonstrated that the drag of the hand-cyclist in a road setup increased by 14.1% from 0° to 15° yaw, but the TT setup experienced a maximum drag increase of only 3.3%, from 0° to 5° yaw. Disk wheels were determined as the most influential geometrical factor for both drag and lateral forces between the road (spoked wheels) and TT (disk wheels) hand-cycle setups. The lateral force experienced by the TT hand-cyclist exceeded the drag at 20° yaw by 5.6 times, in comparison to 1.6 times for the road setup at the same yaw angle. Athletes should carefully consider the use of disk wheels if high wind speeds are present at race events, as despite the drag benefits provided by comparison to spoked wheels, lateral forces in excess of the drag forces can be generated at yaw angles of 5° and higher.

Future research on the topic should include dynamic models with rotating wheels. In addition, a variety of wheel designs should be compared to determine the most suitable designs for drag and lateral force reduction. The three wheels of a hand-cyclist interact aerodynamically with the hand-cycle frame and athlete geometries, and remain a key area for further investigation. There is potential for new innovations in wheel design specific to hand-cycling, with new technologies that are unique to hand-cycling and not derived or borrowed from able-bodied traditional cycling.

Conflicts of interest

None.

Acknowledgements

The authors acknowledge the support of the College of Engineering and Informatics at the National University of Ireland, Galway. The authors acknowledge the collaboration with Paralympics Ireland, Cycling Ireland and Sport Ireland Institute, along with the technical support team of the Department of the Built Environment at Eindhoven University of Technology: Jan Diepens, Geert-Jan Maas, and Stan van Asten. The authors acknowledge the SFI/HEA Irish Centre for High-End Computing (ICHEC) for the provision of computational facilities and support, and also acknowledge partnership with ANSYS CFD. This project did not receive any specific grant from funding agencies in the public, commercial or not-for-profit sectors.

References

ANSYS Fluent, 2015. ANSYS Fluent Theory Guide. Release 16.1 Documentation. ANSYS Inc.

ATI Industrial Automation, 2018. F/T Sensor Delta. Retrieved April 04, 2018, from. www.ati-ia.com/app_content/Documents/9230-05-1330.auto.pdf.

Barlow, J.B., Rae, W.H., Pope, A., 1999. In: Low-speed Wind Tunnel Testing, third ed. John Wiley & Sons.

Barry, N., Burton, D., Crouch, T., Sheridan, J., Luescher, R., 2012. Effect of crosswinds and wheel selection on the aerodynamic behavior of a cyclist. In: 9th Conference of the International Sports Engineering Association, Procedia Eng, 34, pp. 20–25. https://doi.org/10.1016/j.proeng.2012.04.005.

Blocken, B., 2014. 50 years of computational wind engineering: past, present and future. J. Wind Eng. Ind. Aerod. 129, 69–102. https://doi.org/https://doi.org/10.1016/j.jweia.2014.03.008.

Blocken, B., 2015. Computational Fluid Dynamics for urban physics: importance, scales, possibilities, limitations and ten tips and tricks towards accurate and reliable simulations. Build. Environ. 91, 219–245. https://doi.org/10.1016/j.buildenv.2015.02.015.

Blocken, B., Toparlar, Y., 2015. A following car influences cyclist drag: CFD simulations and wind tunnel measurements. J. Wind Eng. Ind. Aerod. 145 (0), 178–186. https://doi.org/10.1016/j.jweia.2015.06.015.

Blocken, B., Toparlar, Y., Andrianne, T., 2016. Aerodynamic benefit for a cyclist by a following motorcycle. J. Wind Eng. Ind. Aerod. 155, 1–10. https://doi.org/https://doi.org/10.1016/j.jweia.2016.04.008.

Crouch, T.N., Burton, D., LaBry, Z.A., Blair, K.B., 2017. Riding against the wind: a review of competition cycling aerodynamics. Sports Eng. 20 (2), 81–110. https://doi.org/10.1007/s12283-017-0234-1.

Defraeye, T., Blocken, B., Koninckx, E., Hespel, P., Carmeliet, J., 2010a. Aerodynamic study of different cyclist positions: CFD analysis and full-scale wind-tunnel tests. J. Biomech. 43 (7), 1262–1268. https://doi.org/10.1016/j.jbiomech.2010.01.025.

Defraeye, T., Blocken, B., Koninckx, E., Hespel, P., Carmeliet, J., 2010b. Computational fluid dynamics analysis of cyclist aerodynamics: performance of different turbulence-modelling and boundary-layer modelling approaches. J. Biomech. 43 (12), 2281–2287. https://doi.org/10.1016/j.jbiomech.2010.04.038.

Fintelman, D.M., Sterling, M., Hemida, H., Li, F.-X., 2014. The effect of crosswinds on cyclists: an experimental study. In: The 2014 Conference of the International Sports Engineering Association, Procedia Eng, 72, pp. 720–725. https://doi.org/10.1016/j.proeng.2014.06.122.

Fintelman, D.M., Hemida, H., Sterling, M., Li, F.-X., 2015a. CFD simulations of the flow around a cyclist subjected to crosswinds. J. Wind Eng. Ind. Aerod. 144, 31–41. https://doi.org/10.1016/j.jweia.2015.05.009.

Fintelman, D.M., Sterling, M., Hemida, H., Li, F.-X., 2015b. The effect of time trial cycling position on physiological and aerodynamic variables. J. Sports Sci. 414, 1–8. April 2015. https://doi.org/10.1080/02640414.2015.1009936.

Franke, J., Hellsten, A., Schlünzen, H., Carissimo, B., 2010. The best practise guideline for the CFD simulation of flows in the Urban Environment: an outcome of COST 732. In: The Fifth International Symposium on Computational Wind Engineering, pp. 1–10. CWE2010.

García-López, J., Rodríguez-Marroyo, J.A., Juneau, C.-E., Peleteiro, J., Martínez, A.C., Villa, J.G., 2008. Reference values and improvement of aerodynamic drag in professional cyclists. J. Sports Sci. 26 (3), 277–286. https://doi.org/10.1080/02640410701501697.

Godo, M., Corson, D., Legensky, S., 2010. A Comparative Aerodynamic Study of Commercial Bicycle Wheels Using CFD. American Institute of Aeronautics and Astronautics, 2010-1431.

Griffith, M.D., Crouch, T., Thompson, M.C., Burton, D., Sheridan, J., 2014. Computational fluid dynamics study of the effect of leg Position on cyclist aerodynamic drag. The American Society of Mechanical Engineers. J. Fluid Eng. 136. https://doi.org/10.1115/1.4027428.

Haake, S.J., 2009. The impact of technology on sporting performance in Olympic sports. J. Sports Sci. 27 (13), 1421–1431. https://doi.org/10.1080/02640410903062019.

Mannion, P., Toparlar, Y., Blocken, B., Hajdukiewicz, M., Andrianne, T., Clifford, E., 2018. Improving CFD prediction of drag on Paralympic tandem athletes: influence of grid resolution and turbulence model. Sports Eng. 21 (2), 123–135. https://doi.org/10.1007/s12283-017-0258-6.

Menter, F.R., 1994. Two-equation eddy-viscosity turbulence models for engineering applications. AIAA J. 32 (8), 1598–1605. https://doi.org/10.2514/3.12149.

Roache, P.J., 1997. Quantification of uncertainty in computational fluid dynamics. Annu. Rev. Fluid Mech. 29, 123–160. https://doi.org/10.1146/annurev.fluid.29.1.123.

Spalart, P., Allmaras, S., 1992. A one-equation turbulence model for aerodynamic flows. In: 30th Aerospace Sciences Meeting and Exhibit. American Institute of Aeronautics and Astronautics. https://doi.org/10.2514/6.1992-439.

Tew, G.S., Sayers, a. T., 1999. Aerodynamics of yawed racing cycle wheels. J. Wind Eng. Ind. Aerod. 82 (1), 209–222. https://doi.org/10.1016/S0167-6105(99)00034-3.

Thorn, A., 1943. Blockage Corrections in a High Speed Wind Tunnel. ARC R&M 2033.

Tominaga, Y., Mochida, A., Yoshie, R., Kataoka, H., Nozu, T., Yoshikawa, M., Shirasawa, T., 2008. AIJ guidelines for practical applications of CFD to pedestrian wind environment around buildings. J. Wind Eng. Ind. Aerod. 96 (10–11), 1749–1761. https://doi.org/10.1016/j.jweia.2008.02.058.

UCI, 2017. Cycling Regulations, Part 16 Para-Cycling. Internationale Union Cycliste. Retrieved from. http://www.uci.ch/mm/Document/News/Rulesandregulation/16/26/73/16han-E_English.PDF.